Article

Cytoplasmic lattices are megadalton storage complexes in mammalian oocytes

https://doi.org/10.1038/s41586-026-10513-8

Received: 12 September 2025

Accepted: 8 April 2026

Published online: 15 April 2026

Open access

Check for updates

Zeynep Ilgın Kılıç[1], Joyce van Loenhout[1], Marten Chaillet[1], Robert M. van Es[2], Paula Sobrevals Alcaraz[2], Harmjan R. Vos[2], Willem E. M. Noteborn[3] & Miguel Ricardo Leung[1]✉

Mammalian oocytes store proteins for embryonic development on abundant structures called cytoplasmic lattices (CPLs)[1]. However, the mechanisms by which they achieve this are unclear, largely because the molecular composition of the lattices themselves is unknown. Here we use cryo-electron microscopy and artificial intelligence-based modelling to reveal the molecular architecture and protein composition of native CPLs from mouse oocytes. We find that CPLs are formed by at least 13 different proteins that assemble into a megadalton-scale complex, including multiple copies of maternal effect factors such as PADI6 and the subcortical maternal complex. We show that proteins that are essential for early embryonic development are structural components of the CPLs, including the cytoskeletal proteins α-tubulin and β-tubulin, which are incorporated into CPLs as unpolymerized dimers, and an array of ubiquitination factors such as the epigenetic regulator and E3 ligase UHRF1, ubiquitin-conjugating E2 enzymes, and ubiquitin ligase substrate adapters. This represents an elegant molecular mechanism by which oocytes stockpile vital proteins through direct incorporation into highly stable supramolecular assemblies. Our findings provide a structural framework for understanding how disrupting stored maternal factors leads to infertility and developmental defects.

Early embryonic development is driven by macromolecules stored in the egg. These maternal reserves are stockpiled in the developing egg cell—the oocyte—as it grows to be one of the largest cells in the body[2]. Mammalian oocytes are thought to accumulate proteins on CPLs[1,3,4]. CPLs were proposed to represent keratin-like intermediate filaments[5,6] or stored ribosomes[3,7,8], but recent cryo-electron tomography (cryo-ET) studies ruled out these possibilities, showing that CPLs instead have a unique architecture formed by approximately 40-nm-wide filaments that stack to form fibrous bundles[1]. However, the limited resolution (about 30 Å) of the cryo-ET reconstructions precluded direct identification of proteins comprising the CPLs; thus, the exact molecular composition of the CPLs remained unknown.

Current data suggest that CPLs are at least partially comprised of maternal effect factors such as PADI6 and the subcortical maternal complex (SCMC). Disruption of these proteins leads to disappearance of CPLs from the oocyte cytoplasm and to concomitant defects in embryonic development[3,4,9–15], which is caused by destabilization of maternal factors that are thought to be stored on the CPLs, including proteins involved in epigenetic reprogramming and cytoskeletal dynamics[1,3,4,15–17]. However, the lack of any high-resolution structural information on the CPLs means that we do not understand precisely how PADI6 and the SCMC contribute to CPL architecture, nor do we understand how diverse maternal proteins associate with and accumulate on the CPLs. In this study, we report a cryo-electron microscopy (cryo-EM) structure of native CPLs from mouse oocytes, revealing that they consist of maternal factors interacting with cytoskeletal proteins, epigenetic regulators and ubiquitination factors to form megadalton-sized storage complexes.

Structure and composition of native CPLs

To define the molecular architecture and composition of the CPLs, we sought to determine a high-resolution structure by cryo-EM. We leveraged the reported detergent resistance of the CPLs[3,8,15,18,19] and lysed mouse oocytes in a buffer containing 0.5% Triton X-100, then directly plunge-froze the burst oocytes on cryo-EM grids without any further purification, enrichment or cross-linking steps (Fig. 1a). The morphometry of these ex situ CPLs resembled those of CPLs imaged in situ by cryo-ET; that is, they appeared as sheets of filaments consisting of large globular subunits repeating every 38 nm (Fig. 1a). We used cryo-EM single-particle analysis (SPA) to generate a three-dimensional reconstruction of the CPLs at a resolution of approximately 4.2 Å, into which we built an atomic model of the fundamental repeat of the CPLs consisting of 13 different proteins with a combined molecular weight of more than 3 MDa (Fig. 1b–d, Extended Data Figs. 1–4, Extended Data Table 1, Methods and Supplementary Figs. 1–12).

We find that CPLs consist of multiple copies of PADI6 and the SCMC proteins NLRP5 (also known as MATER), TLE6, OOEP (also known as FLOPED), KHDC3 (also known as FILIA), ZBED3 and NLRP4F. In addition, we find that several maternal factors are directly incorporated into the structure of the CPLs, including: NLRP14; ubiquitin ligase substrate adapters of the F-box/WD repeat-containing (FBXW) family;

[1]Hubrecht Institute, Royal Netherlands Academy of Arts and Sciences and University Medical Centre Utrecht, Utrecht, The Netherlands. [2]Center for Molecular Medicine, University Medical Center Utrecht, Oncode Institute, Utrecht, The Netherlands. [3]Netherlands Centre for Electron Nanoscopy (NeCEN), Leiden University, Leiden, The Netherlands. ✉e-mail: m.leung@hubrecht.eu

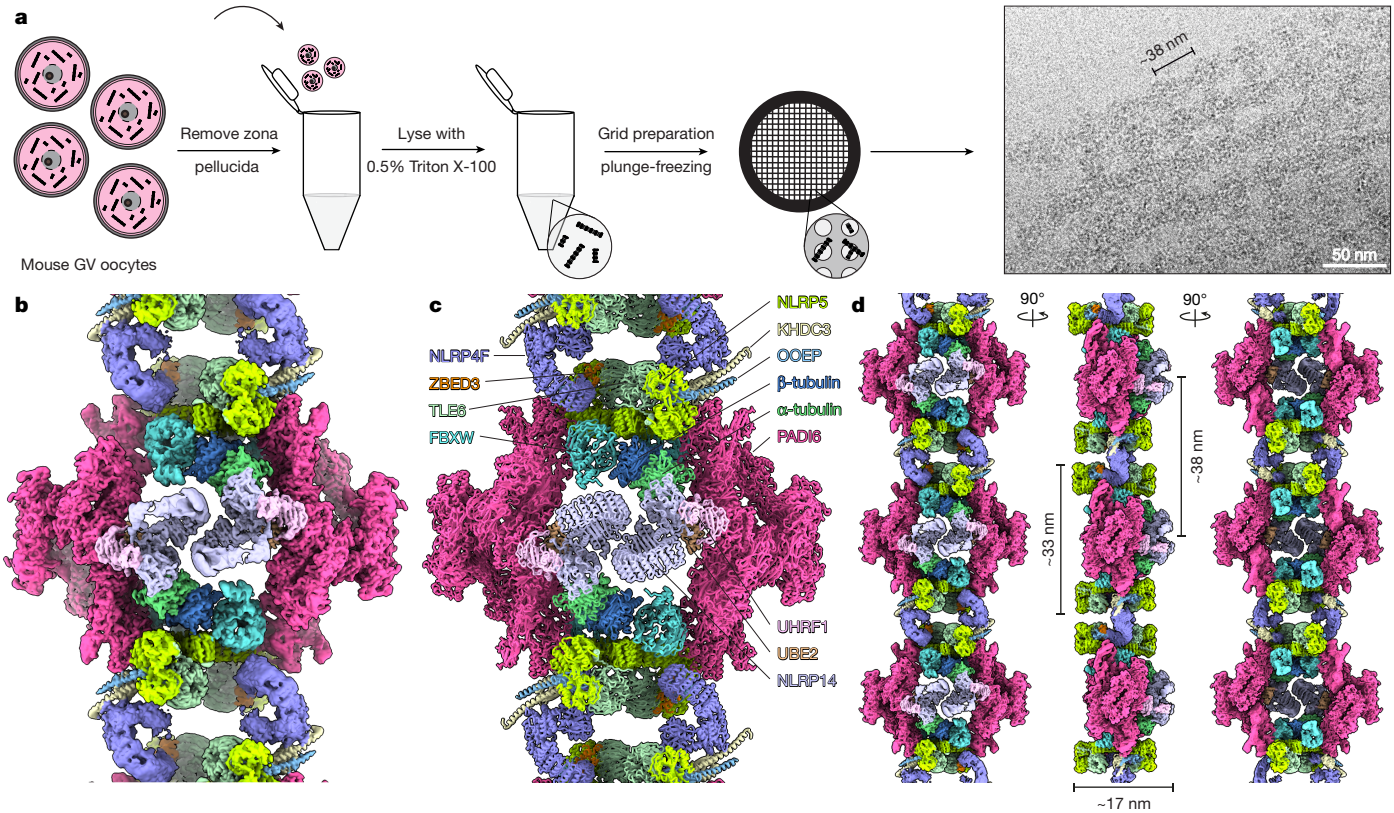


Fig. 1 | Structure and composition of native CPLs from mouse oocytes. **a**, Schematic diagram summarizing the workflow used for preparing and imaging native CPLs by cryo-EM. GV, germinal vesicle. **b**, Composite map showing one CPL globular repeat. This map was generated by duplicating the stitched map of the asymmetric unit around the symmetry axis, followed by fitting into the consensus map obtained before symmetry expansion. **c**, Atomic model of one CPL globular repeat with identified proteins labelled. **d**, Composite map of a CPL filament showing three globular repeats of the CPLs generated by fitting three copies of the globular repeat into the subtomogram average (EMD-16458)[1].

ubiquitin-conjugating E2 (UBE2) enzymes; the epigenetic regulator UHRF1; and the cytoskeletal proteins α-tubulin and β-tubulin, which are incorporated into CPLs as unpolymerized dimers (Fig. 1c, Extended Data Fig. 4 and Supplementary Figs. 1–12). PADI6, NLRP5, TLE6 and OOEP could be readily identified based on similarity of cryo-EM densities to previously reported structures of purified human PADI6 or reconstituted mouse core SCMC (Extended Data Fig. 3b). To identify the other SCMC densities, we fitted candidate proteins based on literature and found that KHDC3, ZBED3 and NLRP4F fit unambiguously into our maps. NLRP14, FBXW, UBE2, UHRF1 and tubulin were identified using a 'visual proteomics' approach involving automated fitting of an AlphaFold structure library derived from proteins identified in published oocyte proteomes (Extended Data Fig. 3b and Methods).

To add further confidence to the assignment of CPL protein components, we used a combination of fold-based and sequence-based identification strategies that leverage recent machine-learning enabled modelling tools (Extended Data Fig. 3c, Methods and Supplementary Figs. 1–12). We first used CryoAtom[20] to automatically build a model into our cryo-EM map without any provided input sequence. We then used the fragments built by CryoAtom as inputs to FoldSeek[21] to search the *Mus musculus* AlphaFold database for the most structurally similar proteins. In parallel, for regions with visible side-chain densities, we used CryoAtom fragments as inputs to findMySequence[22], which assesses side-chain probabilities at each position based on cryo-EM density and subsequently queries a sequence database (in this case, the entire *M. musculus* proteome) to find the most likely candidate.

Identification of CPL component proteins (or protein families in the case of tubulin, FBXW and UBE2) is unambiguous from the cryo-EM densities (Supplementary Figs. 1–12) and is supported by mass spectrometry analysis of burst oocytes showing that all assigned proteins are highly abundant in the sample (Extended Data Fig. 5 and Supplementary Table 1). Furthermore, our assignments are consistent with extensive published functional evidence, including immunofluorescence-based colocalization, co-immunoprecipitation, co-depletion and proteomics on oocytes from both wild-type and gene-disrupted mice[1,3,8–16,19,23–25] (Supplementary Table 2).

PADI6 oligomers scaffold the CPLs

Our structure shows that PADI6, an oocyte-specific member of the peptidyl arginine deiminase family that is highly abundant in mammalian oocytes, assembles into large ring-shaped oligomers on the sides of each globular repeat of the CPL (Fig. 2a). Within the PADI6 rings, individual PADI6 molecules homodimerize through a head-to-tail mechanism resembling the one seen in crystal structures of human PADI6[26] and the related family member PADI4[27] (Fig. 2b and Extended Data Fig. 4d). Each PADI6 ring is formed by five PADI6 homodimers further interacting through their N-terminal immunoglobulin-like domains in a manner that resembles a spiral staircase, with every dimer rotated around 104° and shifted around 32 Å relative to its neighbour (Fig. 2c,d). The dimers at the top and bottom of the ring further interact with proteins of the SCMC, the other major structural component of the CPLs.

Fitting our SPA-derived models into a recent in situ subtomogram average of CPLs[1] reveals that the PADI6 ring is likely to have an important role in higher-order assembly of CPL filaments into fibrous bundles (Extended Data Fig. 6a). We find that there are two types of contacts between individual filaments within a bundle: (1) a 'front-to-back' interaction in which PADI6 rings from adjacent filaments are bridged by unidentified proteins (Extended Data Fig. 6b); and (2) a 'back-to-back'

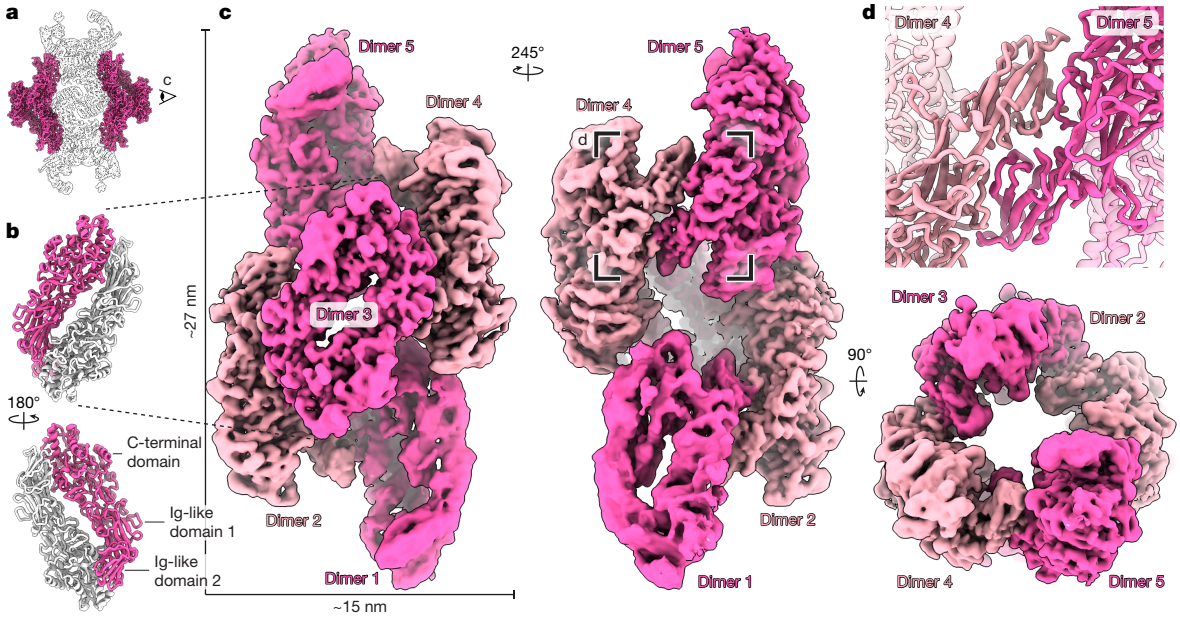


Fig. 2 | PADI6 forms large ring-shaped oligomers. a, Atomic model of one CPL globular repeat with only PADI6 coloured. **b**, Atomic model of the PADI6 dimer. Ig, immunoglobulin. **c**, Cryo-EM maps of a PADI6 ring consisting of 5 dimers arranged in a spiral staircase, with each dimer rotated about 104° and shifted about 32 Å relative to its neighbour. **d**, Contacts between the immunoglobulin-like domains of PADI6 molecules from neighbouring dimers.

interaction seemingly mediated by direct interaction of the PADI6 rings from neighbouring filaments (Extended Data Fig. 6c).

PADI6 therefore acts as an essential structural scaffolding element of the CPLs, explaining why PADI6 disruption leads to loss of CPLs[1,3,8,9,15] (Supplementary Table 2) and why PADI6 defects cause female infertility or imprinting disorders in humans[28–31]. This structural role is likely to be the primary function of PADI6; unlike other PADI proteins, which normally catalyse the post-translational conversion of arginine into citrulline, PADI6 is catalytically inactive in vitro, and female mice with a mutation in the putative PADI6 active site are fertile and produce normal litters[3,31,32].

SCMC proteins mediate filament assembly

SCMC proteins bridge PADI6 rings at the top and bottom of every globular repeat, thereby forming the interface between neighbouring repeats in a filament (Fig. 3a). Previous studies point towards the existence of a core SCMC consisting of NLRP5, TLE6, OOEP and possibly KHDC3[33]; however, accessory proteins ZBED3 and NLRP4F are also proposed to be part of the SCMC[12,14]. We find that all these proposed members of the SCMC are bona fide structural components of the CPLs.

SCMC components assemble into two discrete subcomplexes, which we refer to as type I and II complexes, that dimerize through the leucine-rich repeat (LRR) domain of NLRP5 (Fig. 3b). Both types of SCMC subcomplexes contain NLRP5, TLE6 and OOEP, and type I additionally contains ZBED3 and type II contains KHDC3 (Fig. 3b). NLRP4F proteins bridge one type I subcomplex and one type II subcomplex from neighbouring repeats, giving the CPLs a chain-like appearance (Fig. 3a,c). NLRP4F interacts with an OOEP–KHDC3 heterodimer through its N-terminal pyrin and NACHT domains, and the tip of its C-terminal LRR domain interacts with an OOEP–ZBED3 heterodimer (Fig. 3b,c).

Our results suggest that SCMC proteins are crucial for CPL assembly and integrity; indeed, disruption of NLRP5, TLE6, OOEP, KHDC3, ZBED3 and NLRP4F all lead to the disappearance of CPLs and to early embryonic arrest[1,10–14,19] (Supplementary Table 2). Our findings are consistent with in vitro reconstitution experiments suggesting that NLRP5, TLE6, and OOEP form a core SCMC[33], and the organization of these proteins within native CPLs closely resembles their arrangement in reconstituted subcomplexes (Extended Data Fig. 4e). Our model also explains why disrupting ZBED3 or NLRP4F leads to CPL loss and developmental failure even though the core SCMC does not appear to be affected[12,14]. Thus, we are now able to define the composition and organization of the native SCMC and to understand how its components interact with PADI6 to form the elaborate architecture of the CPLs.

Tubulin heterodimers are stored in CPLs

Recent work suggests that proteins needed by the early embryo are stored on the CPLs[1,3], but precisely how this occurs is unclear. Here we show that several such proteins are in fact structural components of the CPLs, including NLRP14, α-tubulin, β-tubulin, epigenetic regulators and ubiquitination factors (Fig. 4a).

Tubulin is embedded within the CPLs as unpolymerized α-tubulin–β-tubulin (α/β-tubulin) heterodimers, which are capped on both ends to prevent polymerization (Fig. 4b). At the resolution of our current maps, we cannot confidently assign specific tubulin isoforms and have instead tentatively modelled the most abundant α-tubulin (TUBA1A) and β-tubulin (TUBB4B) detected in our samples by mass spectrometry (Extended Data Fig. 5 and Supplementary Table 1). NLRP14 binds α-tubulin to cap the minus end, and NLRP5 and an FBXW protein interact with β-tubulin to cap the plus end. Using 3D classification, we were able to recover particles in which additional FBXW molecules interact with the plus end of β-tubulin (Extended Data Fig. 7). The conformation of the tubulin dimer within the CPLs resembles the curved conformation[34] (Fig. 4c), probably because there are no lattice contacts to restrain it in the straight conformation[35].

There are two tubulin heterodimers in each globular 38-nm repeat (one heterodimer in each asymmetric unit). Given that CPLs occupy 5–10% of the oocyte cytoplasm[1], this would represent a pool on the order of 10^9 to 10^{10} tubulin heterodimers, a concentration in the micromolar range. Multiple studies have reported decreased tubulin levels or cytoskeletal disorganization associated with loss of the CPLs, although these have generally been interpreted as indirect effects[1,3,15,16,25]. Our structure clearly explains these data and provides a molecular mechanism for how oocytes can accumulate and store tubulin at levels much

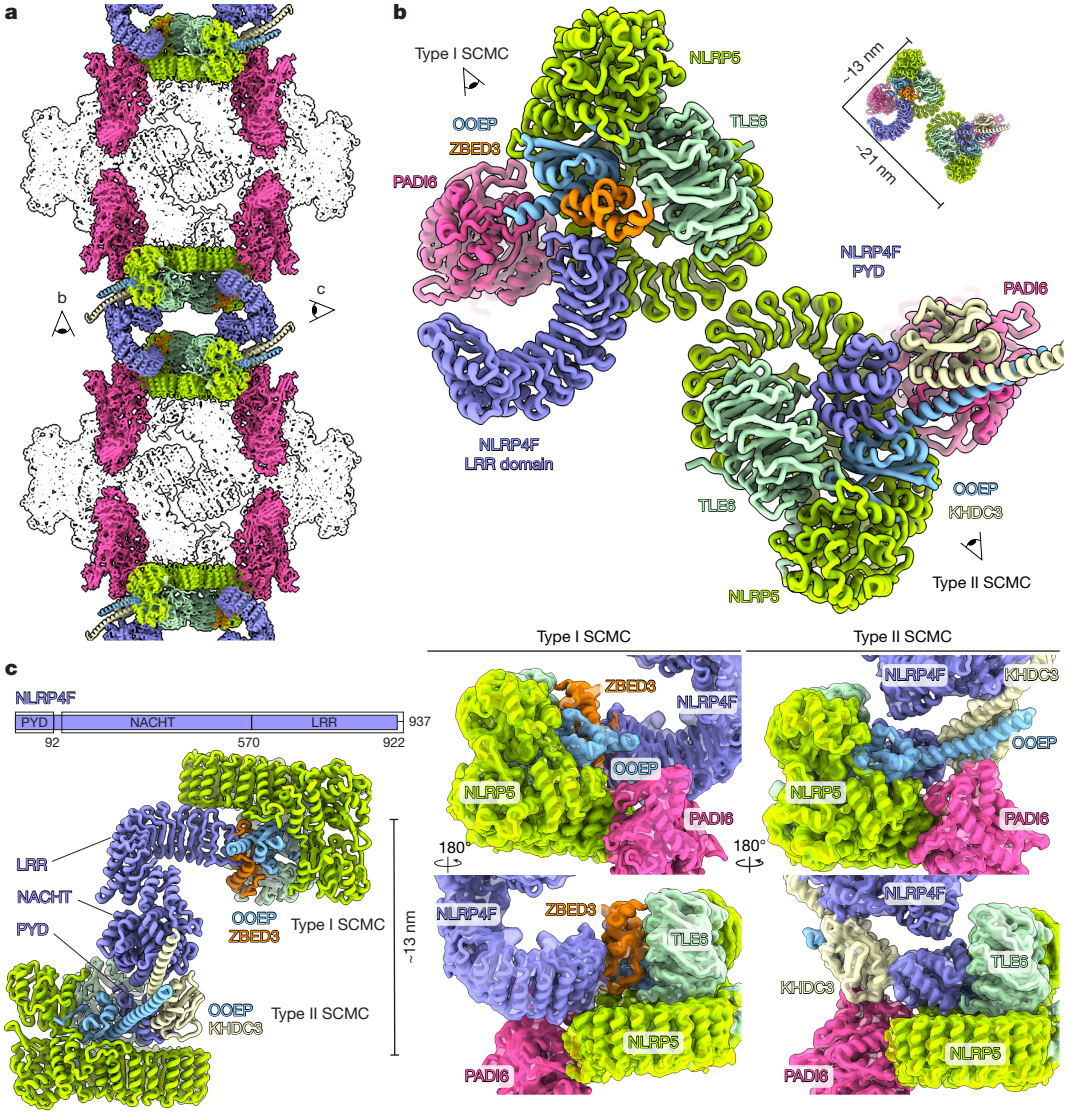


Fig. 3 | SCMC proteins mediate filament assembly. a, Atomic model of two CPL globular repeats with SCMC proteins coloured, along with PADI6 molecules directly interacting with them. **b**, Top, view along the axis of the CPL filament showing two types of SCMC subcomplexes that coexist in native CPLs. Type I subcomplexes consist of NLRP5, TLE6, OOEP and ZBED3, whereas type II subcomplexes contain NLRP5, TLE6, OOEP and KHDC3. Bottom, details of interactions between SCMC components and PADI6, illustrating how the type I subcomplex interacts with the tip of the LRR domain of NLRP4F, whereas the type II subcomplex interacts with the pyrin and NACHT domains of NLRP4F. PYD, pyrin domain. **c**, Top, domain organization of NLRP4F, with boxes indicating residues modelled in the deposited structure. Bottom, view from the side of the CPL filament, showing how NLRP4F bridges one type I subcomplex and one type II subcomplex from neighbouring globular repeats.

higher than in somatic cells[36,37]. Thus, the CPLs represent the maternal reservoir for tubulin, which is necessary for the drastic cytoskeletal reorganization in the zygote and early embryo.

CPLs contain ubiquitination factors

We find an array of ubiquitination factors within the CPLs (Fig. 4a). Within each asymmetric unit, we find one molecule of the E3 ligase and epigenetic regulator UHRF1, one molecule of a ubiquitin-conjugating E2 (UBE2) enzyme, and up to three molecules of FBXW family ubiquitin ligase substrate adapters (Extended Data Fig. 7). We have tentatively modelled the E2 enzyme as UBE2D3 and the FBXW proteins as FBXW20 based on their abundance in our mass spectrometry data (Extended Data Fig. 5 and Supplementary Table 1), although we cannot exclude that different family members bind to different subsets of CPLs[1,3].

A heterodimer of UHRF1 and UBE2 is sandwiched between NLRP14 and the PADI6 ring (Fig. 4d). The UHRF1–UBE2 interaction is mediated by the SET- and RING-associated (SRA) domain of UHRF1, which normally recognizes hemimethylated DNA[38], binding to the 'back side' of UBE2 (Fig. 4e). This configuration would leave the active site of UBE2 exposed (Fig. 4e)[39], although it is unclear whether it is enzymatically active within the CPLs. The ubiquitin-like (UBL) domain of UHRF1 additionally interacts with the NACHT domain of NLRP14 (Fig. 4d). Indeed, deletion of the UBL domain abrogates the binding between UHRF1 and NLRP14[25], demonstrating that this interaction is important for the stability of the complex.

Our findings explain how UHRF1 is sequestered stably in the oocyte cytoplasm, which is essential for regulating methylation patterns in the early embryo[17,25,40,41]. Furthermore, our structures show why the cytoplasmic localization of UHRF1 is dependent on NLRP14[25,40,42], and why depletion of either protein leads to loss of CPLs[16,25], pointing at an important noncanonical role for UHRF1—and probably FBXW and UBE2—in the oocyte as a structural component of these storage complexes.

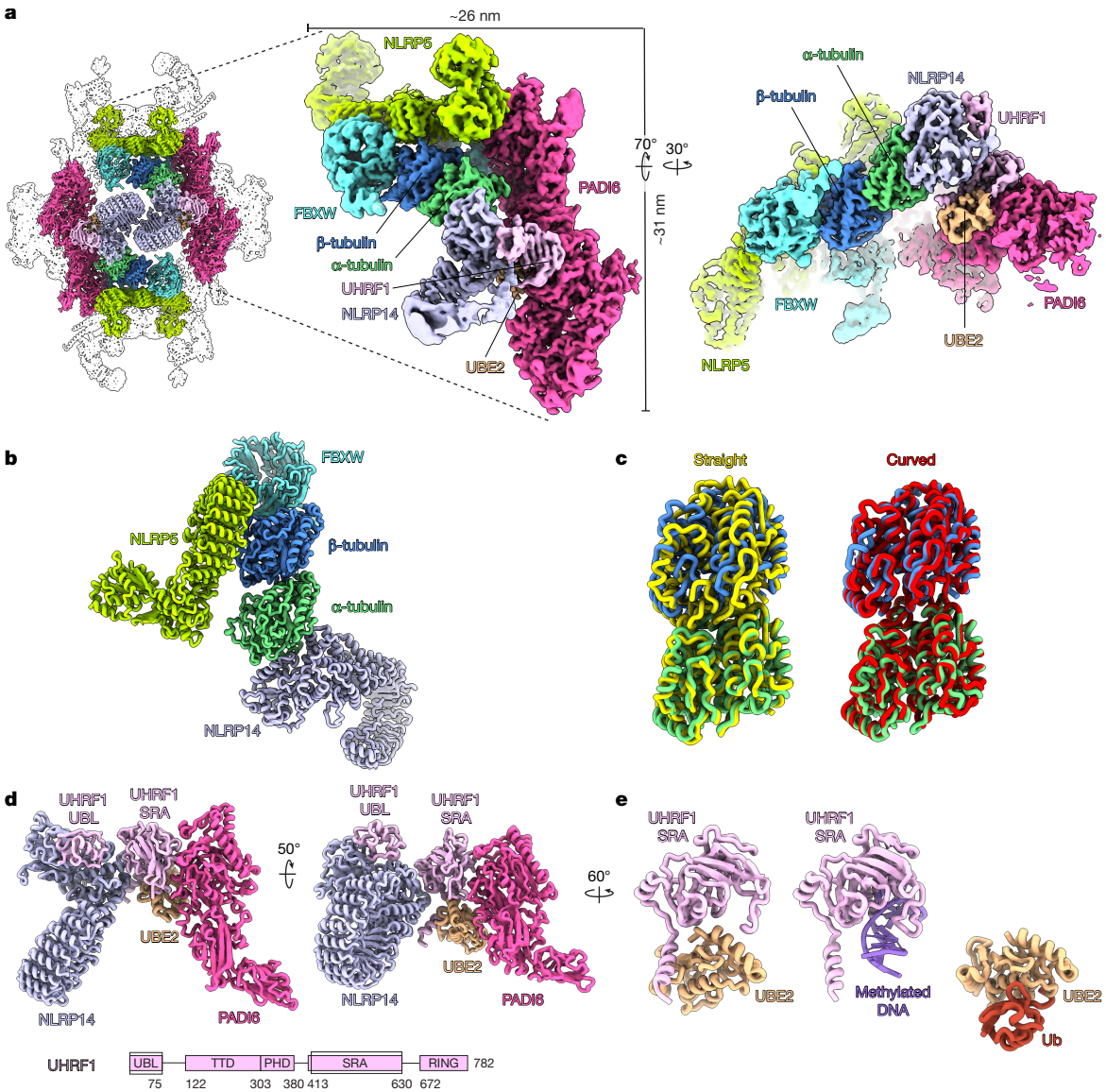


Fig. 4 | Tubulin and ubiquitination factors are integral structural components of CPLs. a, Left, atomic model of one CPL globular repeat with stored maternal factors coloured, along with the NLRP5 and PADI6 molecules directly interacting with them. Middle and right, cryo-EM maps of the maternal storage subcomplex. **b**, The α/β-tubulin heterodimer and its interaction partners in the CPLs. **c**, Comparison of the α/β-tubulin heterodimer in the CPLs with α/β-tubulin in the straight (Protein Data Bank (PDB) 6DPV[35]) or curved conformation (PDB 4I4T[34]). **d**, UHRF1 and a UBE2 enzyme are sandwiched between NLRP14 and PADI6. The domain organization of UHRF1 is shown, with boxes indicating residues modelled in the deposited structure. PHD, plant homeodomain; TTD, tandem Tudor domain. **e**, Left, interaction between the UHRF1 SRA domain and UBE2 within the CPLs. Middle, structure of a complex between the UHRF1 SRA domain and hemimethylated DNA (PDB 3CLZ[38]). Right, structure of a UBE2–ubiquitin (Ub) complex (PDB 1FXT[39]).

Discussion

We have revealed the molecular composition of oocyte CPLs. Our structure also explains how proteins essential for the early embryo are stored on CPLs, demonstrating that they directly interact with oocyte-specific proteins to assemble into highly structured, highly stable megadalton-scale storage complexes. Proteins within the lattice are protected from degradation, consistent with data showing that tubulin and UHRF1 protein levels decrease when CPLs are lost[1,3,16,25,42]. Incorporation into the CPLs also regulates subcellular localization, as in the case of UHRF1, which needs to be sequestered in the cytoplasm to permit proper epigenetic reprogramming of the embryo[17,25,40,41]. Entrapment within the lattice may allow maternal factors such as tubulin to accumulate to very high levels (micromolar concentration) by circumventing autoregulation pathways that rely on sensing free soluble protein. In the case of tubulin, CPL formation may also serve to maintain a pool of non-polymerized tubulin that can be easily mobilized after fertilization despite tubulin concentration exceeding the critical concentration for polymerization.

Our finding that proteins of the ubiquitination pathway, including E2 enzymes and E3 ligase substrate adapters, are also components of the CPLs suggests that these structures may also function in regulating protein turnover during the oocyte-to-embryo transition. Sequestration of ubiquitination factors in the CPLs may prevent their activity during oogenesis, allowing large quantities of maternal factors to accumulate. Their subsequent release during CPL disassembly may then be important for regulating the timed degradation of maternal factors in the early embryo[2]. Among the factors that need to be degraded are components of the CPLs themselves, such as PADI6 and the SCMC[11–14,23,24],

which may be less important when the embryo becomes self-sustaining in later stages of development.

We can only speculate how CPL disassembly is triggered during early embryogenesis to enable release of its constituent proteins. Multi-body refinement of particles extracted with a larger box size suggests that there is considerable flexibility in the CPL filament, manifesting mainly as relative bending motions between neighbouring CPL globular repeats (Extended Data Fig. 8), although how this contributes to eventual disassembly remains to be tested. One possibility is that activation of transcription or translation in the embryo may lead to the expression of a protein that destabilizes the CPLs, either through direct binding or by inducing post-translational modifications that lead to CPL disassembly. Along these lines, it is interesting to note that the CPLs have large pockets that could feasibly accommodate the binding of additional proteins (Extended Data Fig. 9). Understanding how the CPLs assemble during oogenesis and disassemble in the early embryo will be important topics for further study.

Online content

Any methods, additional references, Nature Portfolio reporting summaries, source data, extended data, supplementary information, acknowledgements, peer review information; details of author contributions and competing interests; and statements of data and code availability are available at https://doi.org/10.1038/s41586-026-10513-8.

1. Jentoft, I. M. A. et al. Mammalian oocytes store proteins for the early embryo on cytoplasmic lattices. *Cell* **186**, 5308–5327.e25 (2023).
2. Li, L., Zheng, P. & Dean, J. Maternal control of early mouse development. *Development* **137**, 859–870 (2010).
3. Williams, J. P. C. et al. Dissecting PADI6 function defines oocyte cytoplasmic lattices as regulatory hubs for fundamental cellular processes. Preprint at *bioRxiv* https://doi.org/10.1101/2025.02.21.639491 (2025).
4. Giaccari, C., Cecere, F., Argenziano, L., Pagano, A. & Riccio, A. New insights into oocyte cytoplasmic lattice-associated proteins. *Trends Genet.* **40**, 880–890 (2024).
5. McGaughey, R. W. & Capco, D. G. Specialized cytoskeletal elements in mammalian eggs: structural and biochemical evidence for their composition. *Cell Motil. Cytoskeleton* **13**, 104–111 (1989).
6. Capco, D. G., Gallicano, G. I., McGaughey, R. W., Downing, K. H. & Larabell, C. A. Cytoskeletal sheets of mammalian eggs and embryos: a lattice-like network of intermediate filaments. *Cell Motil. Cytoskeleton* **24**, 85–99 (1993).
7. Burkholder, G. D., Comings, D. E. & Okada, T. A. A storage form of ribosomes in mouse oocytes. *Exp. Cell. Res.* **69**, 361–371 (1971).
8. Yurttas, P. et al. Role for PADI6 and the cytoplasmic lattices in ribosomal storage in oocytes and translational control in the early mouse embryo. *Development* **135**, 2627–2636 (2008).
9. Esposito, G. et al. Peptidylarginine deiminase (PAD) 6 is essential for oocyte cytoskeletal sheet formation and female fertility. *Mol. Cell. Endocrinol.* **273**, 25–31 (2007).
10. Tong, Z.-B. et al. Mater, a maternal effect gene required for early embryonic development in mice. *Nat. Genet.* **26**, 267–268 (2000).
11. Li, L., Baibakov, B. & Dean, J. A subcortical maternal complex essential for preimplantation mouse embryogenesis. *Dev. Cell* **15**, 416–425 (2008).
12. Qin, D. et al. The subcortical maternal complex protein Nlrp4f is involved in cytoplasmic lattice formation and organelle distribution. *Development* **146**, dev183616 (2019).
13. Tashiro, F. et al. Maternal-effect gene *Ces5*/*Ooep*/*Moep19*/*Floped* is essential for oocyte cytoplasmic lattice formation and embryonic development at the maternal–zygotic stage transition. *Genes Cells* **15**, 813–828 (2010).
14. Gao, Z. et al. Zbed3 participates in the subcortical maternal complex and regulates the distribution of organelles. *J. Mol. Cell. Biol.* **10**, 74–88 (2018).
15. Kan, R. et al. Regulation of mouse oocyte microtubule and organelle dynamics by PADI6 and the cytoplasmic lattices. *Dev. Biol.* **350**, 311–322 (2011).
16. Uemura, S. et al. UHRF1 is essential for proper cytoplasmic architecture and function of mouse oocytes and derived embryos. *Life Sci. Alliance* **6**, e202301904 (2023).
17. Cao, Y. et al. Deletion of maternal UHRF1 severely reduces mouse oocyte quality and causes developmental defects in preimplantation embryos. *FASEB J.* **33**, 8294–8305 (2019).
18. Gallicano, G. I., Larabell, C. A., McGaughey, R. W. & Capco, D. G. Novel cytoskeletal elements in mammalian eggs are composed of a unique arrangement of intermediate filaments. *Mech. Dev.* **45**, 211–226 (1994).
19. Kim, B., Kan, R., Anguish, L., Nelson, L. M. & Coonrod, S. A. Potential role for MATER in cytoplasmic lattice formation in murine oocytes. *PLoS ONE* **5**, e12587 (2010).
20. Su, B., Huang, K., Peng, Z., Amunts, A. & Yang, J. CryoAtom improves model building for cryo-EM. *Nat. Struct. Mol. Biol.* **33**, 351–361 (2026).
21. Van Kempen, M. et al. Fast and accurate protein structure search with Foldseek. *Nat. Biotechnol.* **42**, 243–246 (2024).
22. Chojnowski, G. et al. FindMySequence: a neural-network-based approach for identification of unknown proteins in X-ray crystallography and cryo-EM. *IUCrJ* **9**, 86–97 (2022).
23. Wright, P. W. et al. ePAD, an oocyte and early embryo-abundant peptidylarginine deiminase-like protein that localizes to egg cytoplasmic sheets. *Dev. Biol.* **256**, 74–89 (2003).
24. Ohsugi, M., Zheng, P., Baibakov, B., Li, L. & Dean, J. Maternally derived FILIA–MATER complex localizes asymmetrically in cleavage-stage mouse embryos. *Development* **135**, 259–269 (2008).
25. Zhang, W. et al. NLRP14 deficiency causes female infertility with oocyte maturation defects and early embryonic arrest by impairing cytoplasmic UHRF1 abundance. *Cell Rep.* **42**, 113531 (2023).
26. Williams, J. P. C. et al. Structural insight into the function of human peptidyl arginine deiminase 6. *Comput. Struct. Biotechnol. J.* **23**, 3258–3269 (2024).
27. Arita, K. et al. Structural basis for histone N-terminal recognition by human peptidylarginine deiminase 4. *Proc. Natl Acad. Sci. USA* **103**, 5291–5296 (2006).
28. Eggermann, T., Kadgien, G., Begemann, M. & Elbracht, M. Biallelic PADI6 variants cause multilocus imprinting disturbances and miscarriages in the same family. *Eur. J. Hum. Genet.* **29**, 575–580 (2021).
29. Cubellis, M. V. et al. Loss-of-function maternal-effect mutations of *PADI6* are associated with familial and sporadic Beckwith-Wiedemann syndrome with multi-locus imprinting disturbance. *Clin. Epigenetics* **12**, 139 (2020).
30. Begemann, M. et al. Maternal variants in NLRP and other maternal effect proteins are associated with multilocus imprinting disturbance in offspring. *J. Med. Genet.* **55**, 497–504 (2018).
31. Williams, J. P. C. & Walport, L. J. PADI6: What we know about the elusive fifth member of the peptidyl arginine deiminase family. *Philos. Trans. R. Soc. B* **378**, 20220242 (2023).
32. Raijmakers, R. et al. Methylation of arginine residues interferes with citrullination by peptidylarginine deiminases in vitro. *J. Mol. Biol.* **367**, 1118–1129 (2007).
33. Chi, P. et al. Structural basis of the subcortical maternal complex and its implications in reproductive disorders. *Nat. Struct. Mol. Biol.* **31**, 115–124 (2024).
34. Prota, A. E. et al. Molecular mechanism of action of microtubule-stabilizing anticancer agents. *Science* **339**, 587–590 (2013).
35. Zhang, R., LaFrance, B. & Nogales, E. Separating the effects of nucleotide and EB binding on microtubule structure. *Proc. Natl Acad. Sci. USA* **115**, E6191–E6200 (2018).
36. Jentoft, I. M. A. & Schuh, M. Protein storage in oocytes: implications for oocyte quality, embryonic development, and female fertility. *Annu. Rev. Cell Dev. Biol.* **41**, 15–43 (2025).
37. Schultz, R. M., Letourneau, G. E. & Wassarman, P. M. Program of early development in the mammal: changes in the patterns and absolute rates of tubulin and total protein synthesis during oocyte growth in the mouse. *Dev. Biol.* **73**, 120–133 (1979).
38. Avvakumov, G. V. et al. Structural basis for recognition of hemi-methylated DNA by the SRA domain of human UHRF1. *Nature* **455**, 822–825 (2008).
39. Hamilton, K. S. et al. Structure of a conjugating enzyme-ubiquitin thiolester intermediate reveals a novel role for the ubiquitin tail. *Structure* **9**, 897–904 (2001).
40. Yan, R. et al. Dynamics of DNA hydroxymethylation and methylation during mouse embryonic and germline development. *Nat. Genet.* **55**, 130–143 (2023).
41. Maenohara, S. et al. Role of UHRF1 in de novo DNA methylation in oocytes and maintenance methylation in preimplantation embryos. *PLoS Genet.* **13**, e1007042 (2017).
42. Meng, T.-G. et al. NLRP14 safeguards calcium homeostasis via regulating the K27 ubiquitination of Nclx in oocyte-to-embryo transition. *Adv. Sci.* **10**, e2301940 (2023).

Publisher's note Springer Nature remains neutral with regard to jurisdictional claims in published maps and institutional affiliations.

Open Access This article is licensed under a Creative Commons Attribution-NonCommercial-NoDerivatives 4.0 International License, which permits any non-commercial use, sharing, distribution and reproduction in any medium or format, as long as you give appropriate credit to the original author(s) and the source, provide a link to the Creative Commons licence, and indicate if you modified the licensed material. You do not have permission under this licence to share adapted material derived from this article or parts of it. The images or other third party material in this article are included in the article's Creative Commons licence, unless indicated otherwise in a credit line to the material. If material is not included in the article's Creative Commons licence and your intended use is not permitted by statutory regulation or exceeds the permitted use, you will need to obtain permission directly from the copyright holder. To view a copy of this licence, visit http://creativecommons.org/licenses/by-nc-nd/4.0/.

© The Author(s) 2026

Methods

Experimental animals

All mice used in this study were obtained from the surplus animals of the Animal Facility of the Hubrecht Institute, where mice were maintained in a controlled pathogen-free environment in accordance with institutional guidelines. All data provided in this paper were obtained from surplus sexually mature BALB/cN mice. We consulted with the Animal Welfare Body of the Hubrecht Institute (Instantie voor Dierenwelzijn, Hubrecht Institute), who advised us that ethical approval was not necessary for the use of surplus animal carcasses for this project.

Oocyte collection, rupture and plunge freezing of the oocyte lysates

Ovaries dissected from female BALB/cN mice were collected in a 35-mm dish with M2 medium (Sigma Aldrich, M7167) and punctured under a stereomicroscope using 27G needles (AGANI). Liberated oocytes were mechanically denuded from surrounding somatic cells using a mouth pipette attached to pulled microcapillary needles (Sigma Aldrich, Z611263) and assessed for quality. Only the healthy GV oocytes were washed and collected in fresh M2 medium. Zona pellucida was removed from the GV oocytes by passing them through several drops of acidic Tyrode solution (Sigma Aldrich, T1788), and remnants of the acidic Tyrode were washed from the oocytes through several passes with M2 medium. Approximately 60 zona-denuded GV oocytes were then transferred to 20 µl of homemade oocyte rupture buffer (20 mM Tris-HCl pH 7.9, 132 mM sucrose, 24 mM potassium glutamate) supplemented with 0.5% Triton X-100 (Sigma Aldrich, T8787) and 1× complete Protease Inhibitor Cocktail (Roche, 11836153001), then mixed gently to facilitate rupture of the oocytes and dispersal of the cytoplasm. To prepare samples for cryo-EM, ~4 µl of the ruptured oocyte solution was pipetted onto glow-discharged Quantifoil R2/1 200-mesh holey carbon grids and blotted for 6 seconds from the opposite side of the grid using Whatman 1 filter paper. Grids were immediately plunged into an ethane-propane mix (37% ethane) cooled to liquid nitrogen temperature and stored under liquid nitrogen until data collection.

Cryo-EM data collection

Cryo-EM SPA data was collected at the Netherlands Centre for Electron Nanoscopy (NeCEN) using a Titan Krios G1 (ThermoFisher) operated at 300 kV. Movies were acquired on a K3 detector (Gatan) equipped with a BioQuantum energy filter at a slit width of 20 eV. CPLs were manually targeted for imaging and a total of 38,053 movies were collected semi-automatically using SerialEM[43] over 2 separate multi-day sessions on a total of three grids. Data quality was monitored on the fly with Warp[44]. Further details are summarized in Extended Data Table 1.

Cryo-EM data processing

Each globular repeat of the CPLs was treated as a single particle and processed as such (that is, they were not treated as filaments). Initial processing was performed using cryoSPARC[45] Live during acquisition of the first dataset. Movie frames were motion-corrected and dose-weighted using Patch Motion Correction, after which contrast transfer function (CTF) was estimated using Patch CTF Estimation. A few hundred globular repeats were then picked manually and fed into a 2D classification run, with resulting good class averages used as templates for template-based picking. Particle picks were then fed into another round of 2D classification, with particles falling into good classes carried forward for refinement. For initial refinements, cryoSPARC Homogeneous Refinement was used with an approximately 30 Å resolution subtomogram average of the CPLs (EMD-16458) as initial reference. This revealed the presence of *C*2 symmetry and resulted in an approximately 8 Å resolution map that was used as a new reference for subsequent refinements on the whole dataset.

The full dataset was then processed in cryoSPARC v4.7.0 unless otherwise specified. Movies were motion-corrected with Patch Motion Correction and CTF parameters estimated with Patch CTF Estimation. The map obtained from initial processing was used as a template to pick particles, which were then extracted with a box size of 800 and binned 4×. After 2D classification, particles belonging to good classes were fed into Homogeneous Refinement with *C*2 symmetry applied. Particles were then re-extracted with a box size of 800, binned 2×, locally refined, then finally re-extracted again with a box size of 512 without binning.

The particle stack was then symmetry-expanded in *C*2 and the asymmetric unit subsequently locally refined in *C*1. This improved the resolution to about 4.7 Å. The asymmetric unit was then re-centred, and the resulting particles re-extracted. Particles were then exported to RELION-5 using csparc2star.py in the pyem package[46]. After CTF refinement and Bayesian polishing, 3D classification without alignment was performed using masks for the SCMC region, the PADI6 region, and the tubulin subcomplex region. In each case, particles belonging to the best class were used in a final masked local refinement with Blush regularization, which led to resolutions of ~4.2 Å for the SCMC region, ~4.1 Å for the tubulin subcomplex region, and ~4.1 Å for the PADI6 ring (Extended Data Fig. 2). These three locally refined maps were aligned to the consensus map of the asymmetric unit and stitched together using volume maximum in ChimeraX (Extended Data Fig. 3a). Two copies of the asymmetric unit map were then stitched to yield a composite map of the globular repeat. Finally, three copies of the globular repeat map were fit into the subtomogram average (EMD-16458) to generate a composite map of the CPL filament.

Multi-body analysis was performed in RELION-5 (Extended Data Fig. 8). Particles were first imported from a consensus refinement of the globular repeat in cryoSPARC, then re-extracted with a large box size (1,200 pixels, binned 4 times due to computational restraints) and re-refined in *C*1. Particles were then re-centred on the interface between two globular repeats, extracted with a large box size (1,200 pixels, bin 4), and locally refined in *C*1. Multi-body refinement was performed using two generous masks each covering one globular repeat.

Model building and refinement

Maps were postprocessed using LocScale-2.0 to guide interpretation and model building[47]. PADI6, NLRP5, TLE6 and OOEP could be clearly identified in the map based on previously reported structures of purified human PADI6 or reconstituted mouse core SCMC (Extended Data Fig. 3b). Once we had pinpointed the locations of these proteins, we replaced the published structures with mouse AlphaFold predictions[48,49]. To identify the other SCMC densities, we fitted candidate proteins based on the literature and found that KHDC3, ZBED3 and NLRP4F fit unambiguously into our maps. The remaining densities were assigned using a visual proteomics approach. AlphaFold predictions were downloaded for each of the 2,000 most abundant proteins in a previously reported mouse proteome[50]. Each AlphaFold prediction was then rigid body-fit into the segmented density using the colores program[51] in the SITUS package[52]. The fits were then carefully inspected manually to determine the best-fitting candidate. This allowed for definitive identification of tubulin (with α-tubulin and β-tubulin further distinguished by the length of the S9-S10 loop), NLRP14, UHRF1, FBXW and UBE2. The same proteins were also found using DomainSeeker[53], which parses AlphaFold predictions into individual domains, automatically fits these domains into the cryo-EM density, then scores and ranks the top hits.

Other identification strategies employing machine-learning based modelling approaches were also used to increase confidence in protein assignment (Extended Data Fig. 3c and Supplementary Figs. 1–12). The cryo-EM maps were used as input to CryoAtom, which builds an atomic model de novo without any input sequence[20]. Backbone traces from CryoAtom were then used as inputs to FoldSeek[21], querying the mouse AlphaFold database for the most structurally similar proteins.

In parallel, CryoAtom traces in regions with well-resolved side-chain densities were used as input for findMySequence[22], searching against the full mouse reference proteome.

In the case of tubulin, FBXW and UBE2, our map is not sufficiently resolved to confidently determine the specific isoform, and we cannot exclude the possibility that several different isoforms are incorporated in the CPLs across the oocyte cytoplasm. We therefore modelled the most abundant isoform detected in our mass spectrometry results; specifically, TUBA1A, TUBB4B, FBXW20, and UBE2D3 (Extended Data Fig. 5 and Supplementary Table 1). Once proteins had been assigned, we combined chains into a single PDB file in ChimeraX[54] and performed flexible fitting through the Namdinator web server[55]. We then iteratively refined the model in Phenix[56] with manual adjustment in Coot[57]. Structural biology applications used in this project were compiled and configured by SBGrid[58].

Mass spectrometry of burst oocyte samples

Sample preparation. Oocytes from BALBc/N animals were isolated in the same way as described above. For mass spectrometry, four replicates of ~30 GV oocytes were lysed in 20 µl homemade oocyte rupture buffer supplemented with 0.5% Triton X-100 and immediately flash-frozen in liquid nitrogen. Samples were stored at −80 °C until mass spectrometry analysis.

Liquid chromatography–tandem mass spectrometry. Burst oocyte samples were diluted with 50 µl denaturing buffer (100 mM HEPES pH 8, 2% SDS, 10 mM Tris(2-carboxyethyl)phosphine hydrochloride (TCEP) and 40 mM 2-chloro-acetamide) and proteins were cleaned up with the SP3 protocol[59]. Proteins were digested over-night with 0.5 µg Trypsin/LysC (Thermo) in 100 mM HEPES (pH 8), 10 mM $CaCl_2$. After acidification with 2% formic acid, peptides were separated from the beads and were loaded on C-18 stage tips (Affinisep). After elution from the stage tips, acetonitrile was removed using a SpeedVac and the remaining peptide solution was diluted with buffer A (0.1% formic acid) before loading. Peptides were separated on a 25 cm in-house made pulled emitter fused silica column (50 µm internal diameter, Polymicro) packed with 1.9 µm aquapur gold C-18 material (Dr. Maisch) using a 1 h gradient (7% to 80% acetonitrile, 0.1% formic acid), delivered by an Vanquish Neo HPLC (Thermo), and electro-sprayed directly into a Orbitrap Astral Mass Spectrometer (Thermo Scientific). The latter was set in data independent mode with a cycle time of 0.6 second for both Faims CV settings (−45 V and −65 V), in which the full scan was performed at a resolution of 240 K. The precursor mass range for both CVs was 380–980 Th in which the peptides, from an isolation window of 2 Th, were fragmented with a normalized collision energy of 25%.

Data analysis. Raw files were analysed with Spectronaut software (Biognosys, v20.3), with oxidation of methionine set as variable modifications, and carbamidomethylation of cysteine set as fixed modification. The mouse reference proteome from UniProt (retrieved in December 2025) was searched with both the peptide as well as the protein false discovery rate set to 1% and a Pepscore threshold of 0.2. Quantification was done on the MS1 level using the IBAQ algorithm.

Reporting summary

Further information on research design is available in the Nature Portfolio Reporting Summary linked to this article.

Data availability

Cryo-EM maps have been deposited to the Electron Microscopy Data Bank (EMDB) with accession codes: EMD-54838 (composite map), EMD-54839 (consensus map), EMD-54840 (local refinement, PADI6 region), EMD-54841 (local refinement, SCMC region) and EMD-54842 (local refinement, tubulin subcomplex region). The atomic model has been deposited to the Protein Data Bank (PDB) with accession code 9SFP. Mass spectrometry data has been deposited in PRIDE with accession number PXD073451. Previously published structures used for analysis or comparison include: EMD-16458, PDB 6DPV, PDB 4I4T, PDB 3CLZ, PDB 1FXT, PDB 9FMN, PDB 2DEW, PDB 8H93 and PDB 8X7W.

43. Mastronarde, D. N. Advanced data acquisition from electron microscopes with SerialEM. *Microsc. Microanal.* **24**, 864–865 (2018).
44. Tegunov, D. & Cramer, P. Real-time cryo-electron microscopy data preprocessing with Warp. *Nat. Methods* **16**, 1146–1152 (2019).
45. Punjani, A., Rubinstein, J. L., Fleet, D. J. & Brubaker, M. A. CryoSPARC: algorithms for rapid unsupervised cryo-EM structure determination. *Nat. Methods* **14**, 290–296 (2017).
46. Asarnow, D., Palovcak, E. & Cheng, Y. asarnow/pyem: UCSF pyem v0.5 (v0.5). *Zenodo* https://doi.org/10.5281/zenodo.3576630 (2019).
47. Bharadwaj, A., de Bruin, R. & Jakobi, A. J. Confidence-guided cryo-EM map optimisation with LocScale-2.0. Preprint at *bioRxiv* https://doi.org/10.1101/2025.09.11.674726 (2025)
48. Varadi, M. et al. AlphaFold Protein Structure Database in 2024: providing structure coverage for over 214 million protein sequences. *Nucleic Acids Res.* **52**, D368–D375 (2024).
49. Jumper, J. et al. Highly accurate protein structure prediction with AlphaFold. *Nature* **596**, 583–589 (2021).
50. Sun, H. et al. Proteomic profiling reveals the molecular control of oocyte maturation. *Mol. Cell. Proteomics* **22**, 100481 (2023).
51. Chacón, P. & Wriggers, W. Multi-resolution contour-based fitting of macromolecular structures. *J. Mol. Biol.* **317**, 375–384 (2002).
52. Wriggers, W. Conventions and workflows for using Situs. *Acta Crystallogr. D* **68**, 344–351 (2012).
53. Lu, Y., Chen, G., Sun, F., Zhu, Y. & Zhang, Z. De novo identification of protein domains in cryo-electron tomography maps from AlphaFold2 models. Preprint at *bioRxiv* https://doi.org/10.1101/2024.11.21.623534 (2025).
54. Goddard, T. D. et al. UCSF ChimeraX: meeting modern challenges in visualization and analysis. *Protein Sci.* **27**, 14–25 (2018).
55. Kidmose, R. T. et al. Namdinator—automatic molecular dynamics flexible fitting of structural models into cryo-EM and crystallography experimental maps. *IUCrJ* **6**, 526–531 (2019).
56. Afonine, P. V. et al. Real-space refinement in PHENIX for cryo-EM and crystallography. *Acta Crystallogr. D* **74**, 531–544 (2018).
57. Emsley, P., Lohkamp, B., Scott, W. G. & Cowtan, K. Features and development of Coot. *Biol. Crystallogr.* **66**, 486–501 (2010).
58. Herre, C. et al. Introduction of the Capsules environment to support further growth of the SBGrid structural biology software collection. *Acta Crystallogr. D* **80**, 439–450 (2024).
59. Hughes, C. S. et al. Ultrasensitive proteome analysis using paramagnetic bead technology. *Mol. Syst. Biol.* **10**, 757 (2014).
60. Chi, P. et al. Cryo-EM structure of the human subcortical maternal complex and the associated discovery of infertility-associated variants. *Nat. Struct. Mol. Biol.* **31**, 1798–1807 (2024).
61. Quillin, M. L. & Matthews, B. W. Accurate calculation of the density of proteins. *Acta Crystallogr. D* **56**, 791–794 (2000).
62. Carbajal-González, B. I. et al. Conserved structural motifs in the central pair complex of eukaryotic flagella. *Cytoskeleton* **70**, 101–120 (2013).

Acknowledgements Electron microscopy was performed at the Netherlands Centre for Electron Nanoscopy (NeCEN), with initial screening performed at the Utrecht University Electron Microscopy Centre (UU-EMC). We thank L. Renault for management of NeCEN; S. C. Howes, C. Schneijdenberg, M. Bergmeijer, S. Turner and E. Betz-Güttner for management and maintenance of the UU-EMC; and F. Mattiroli and G. Kops for critical reading of the manuscript. This work was funded by the Hubrecht Institute and enabled by exceptional support from the Institute's support departments and scientific facilities, particularly the IT Department and the Animal Facility. P.S.A. and H.R.V. are supported by Oncode Accelerator, which is funded by the Dutch National Growth Fund (NGF).

Author contributions Z.I.K. and M.R.L. prepared samples for cryo-EM and mass spectrometry. R.M.v.E., P.S.A. and H.R.V. performed mass spectrometry analysis. Z.I.K., J.v.L., M.C., W.E.M.N. and M.R.L. collected cryo-EM data. Z.I.K. and M.R.L. processed cryo-EM data and wrote the manuscript with input from all authors.

Competing interests The authors declare no competing interests.

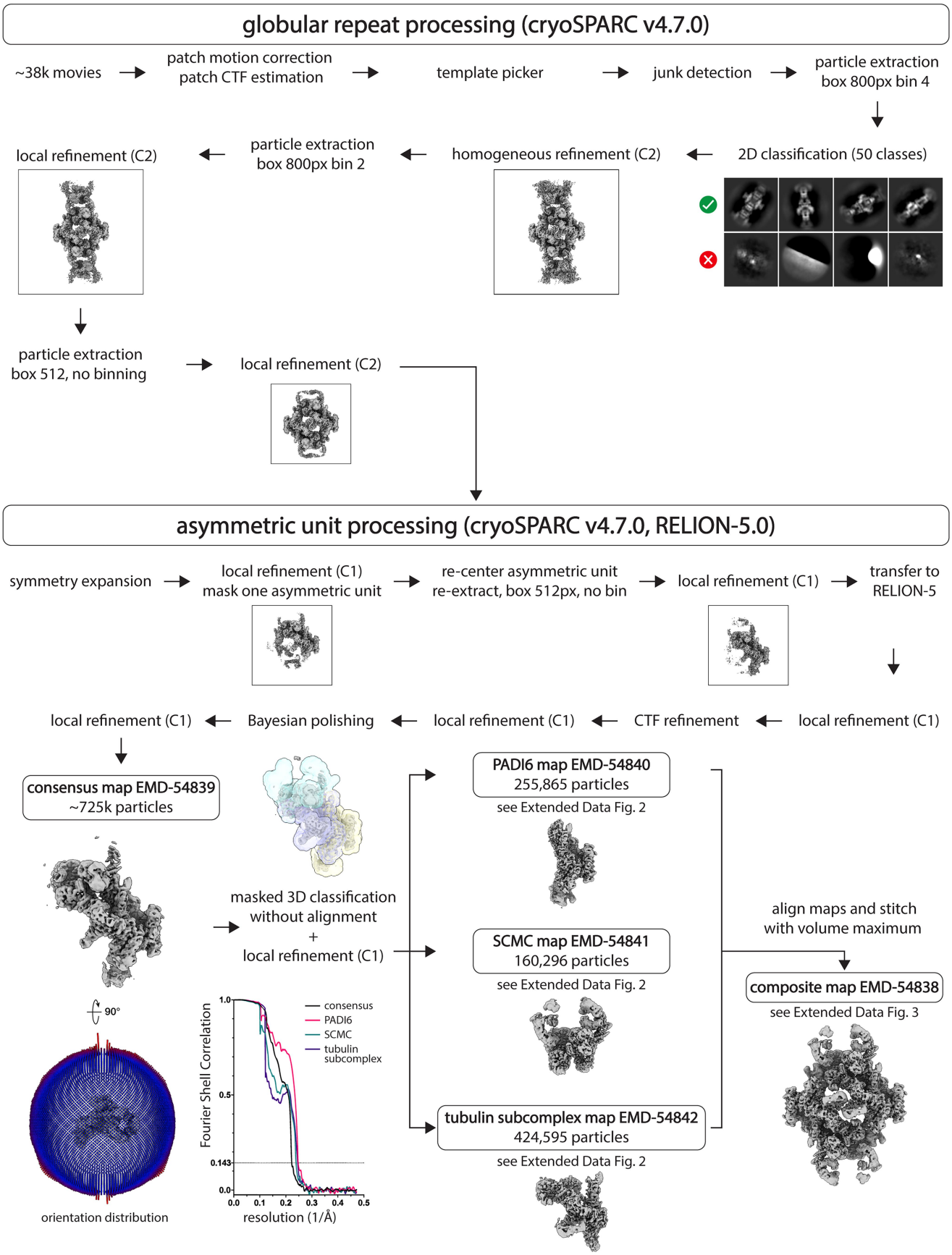
Additional information

Supplementary information The online version contains supplementary material available at https://doi.org/10.1038/s41586-026-10513-8.

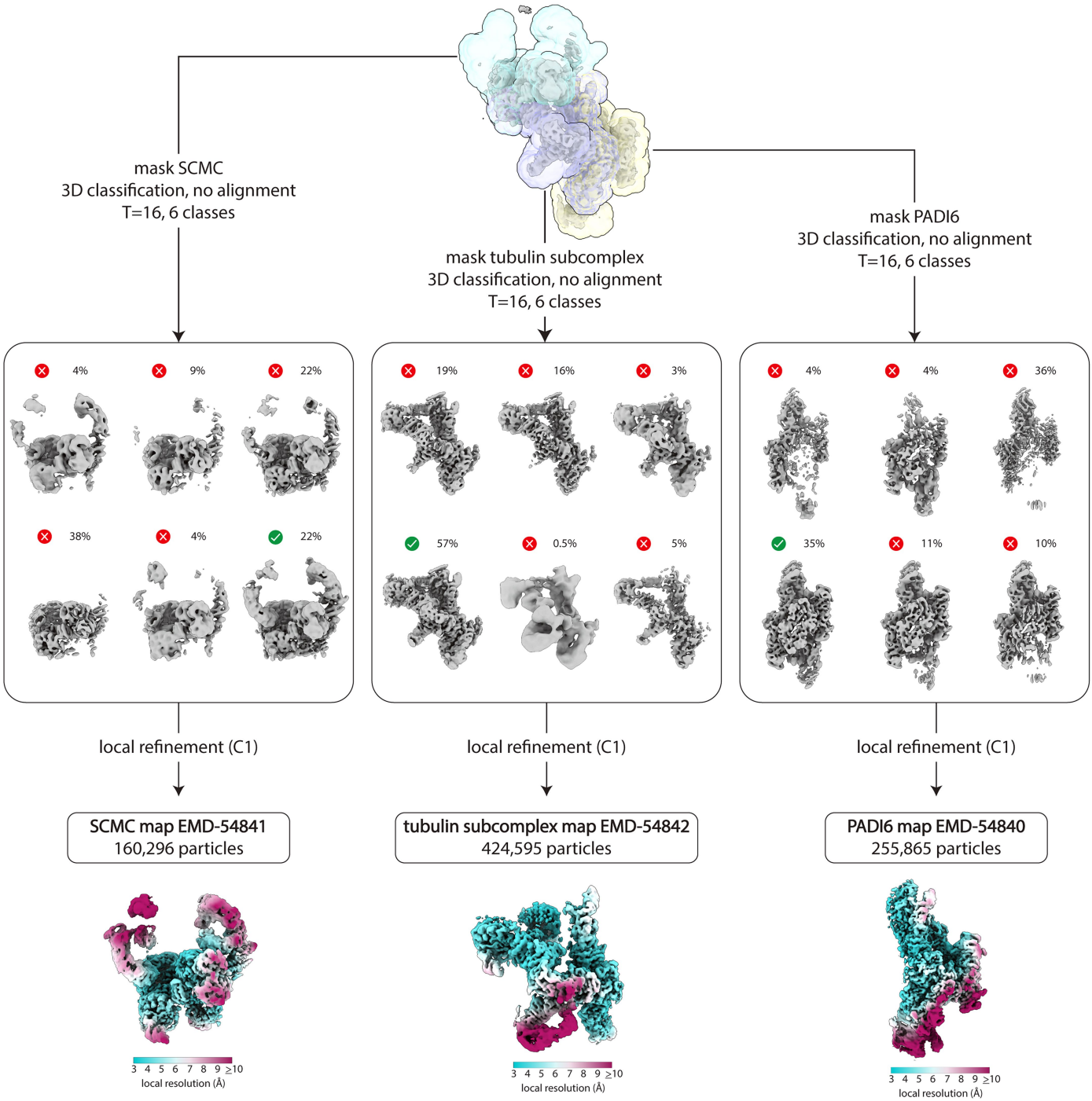
Correspondence and requests for materials should be addressed to Miguel Ricardo Leung.

Peer review information *Nature* thanks Matthias Geyer, Hiroyuki Sasaki and the other, anonymous, reviewer(s) for their contribution to the peer review of this work. Peer review reports are available.

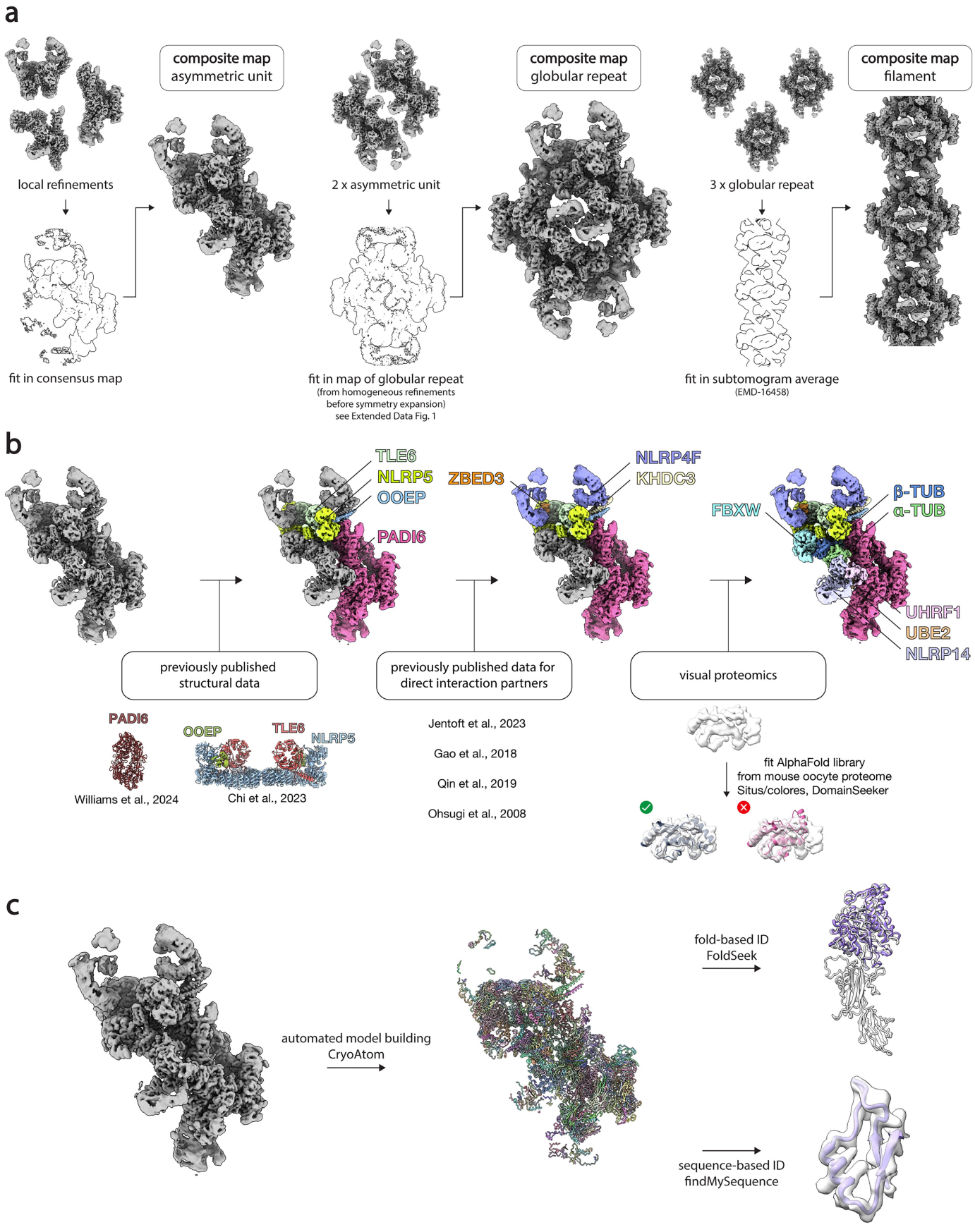
Reprints and permissions information is available at http://www.nature.com/reprints.



Extended Data Fig. 1 | Cryo-EM single particle analysis workflow used to resolve the cytoplasmic lattices (CPLs). See Methods for details.

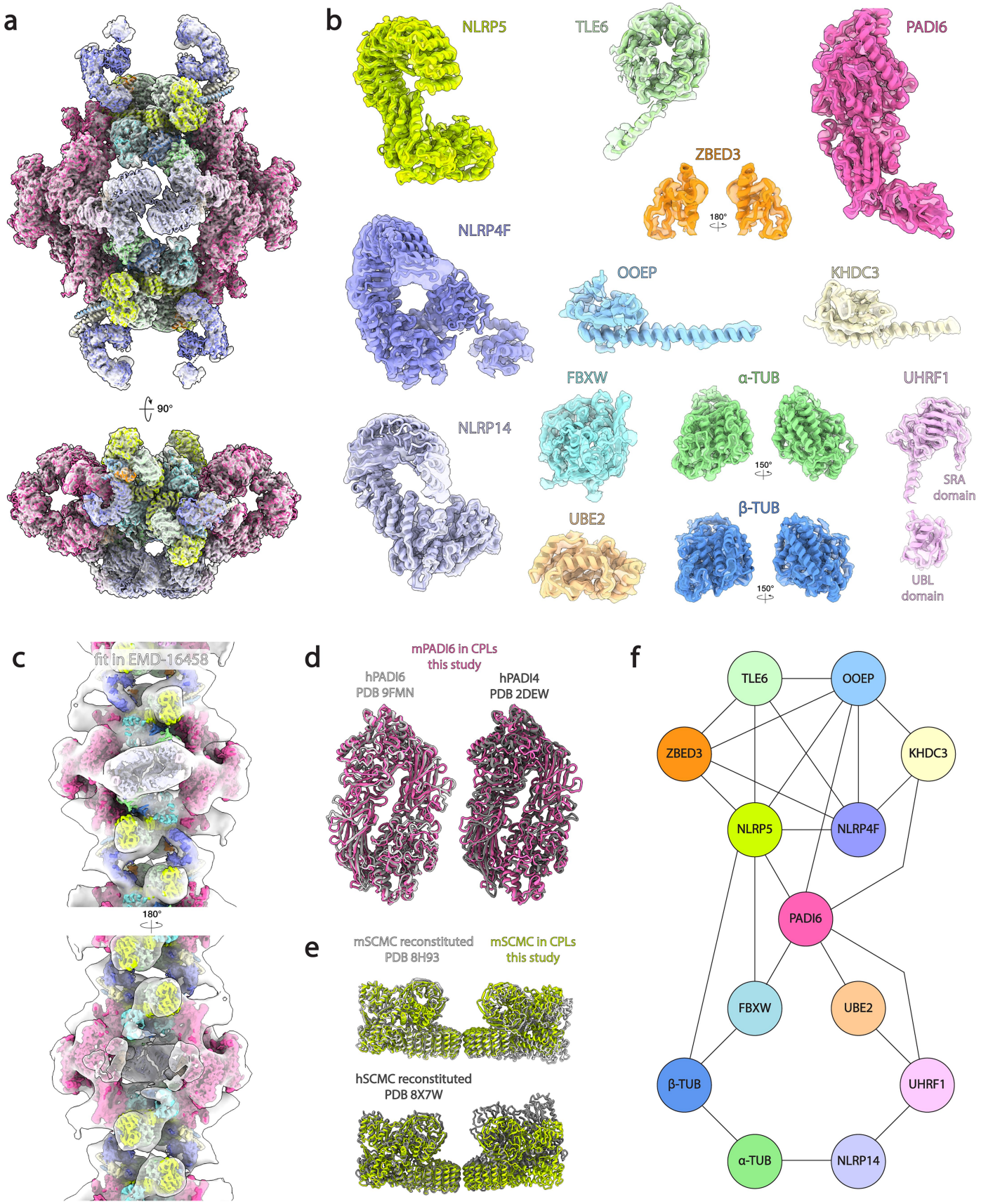


Extended Data Fig. 2 | Details of masked three-dimensional classification and local refinements for the SCMC, tubulin subcomplex, and PADI6 regions. After symmetry expansion, re-centering, and C1 local refinement, the asymmetric unit was divided into three regions with masks covering the SCMC, tubulin subcomplex, and PADI6 ring. For each region, we performed masked 3D classification without image alignment (6 classes, T = 16). The single best-resolved class was selected in each case and the particles therein carried forward to a C1 local refinement.



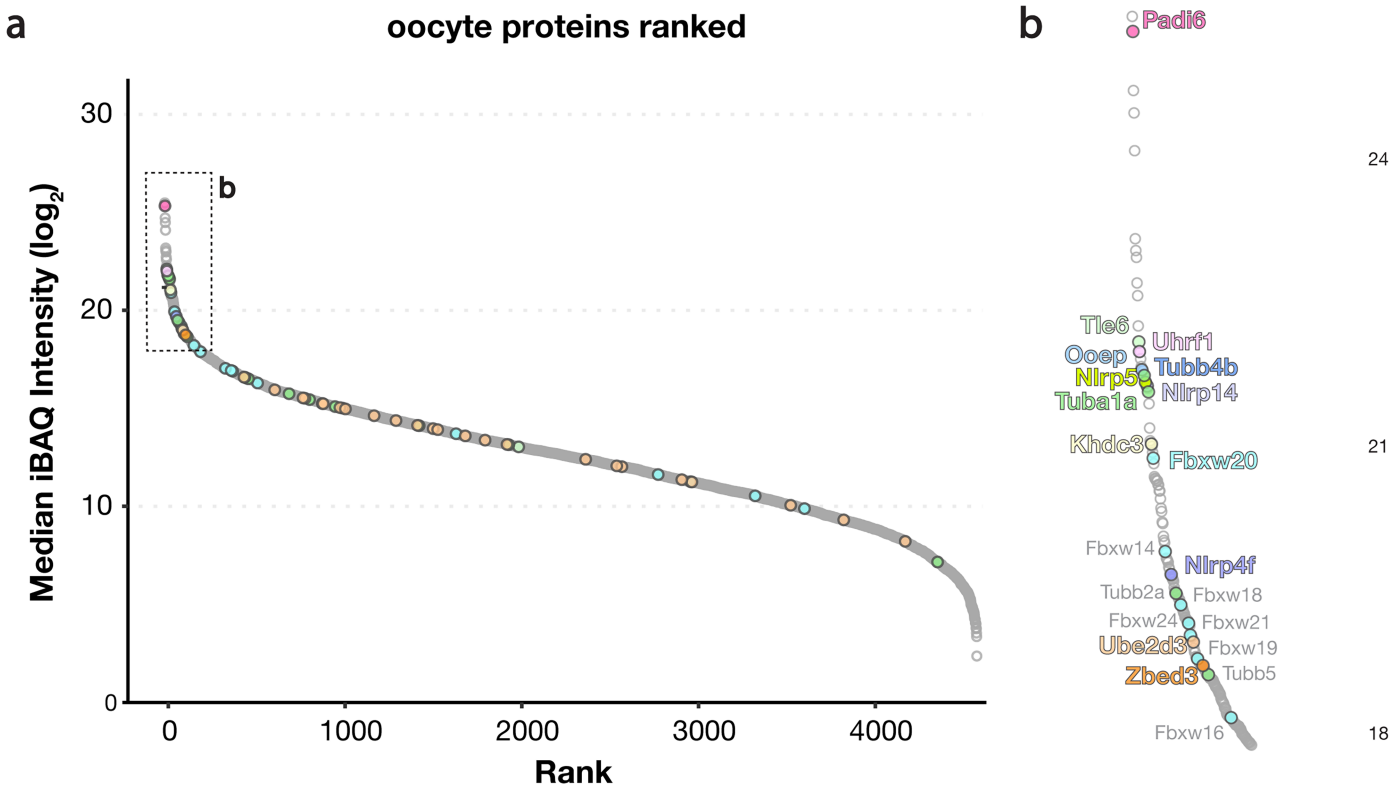
Extended Data Fig. 3 | See next page for caption.

Extended Data Fig. 3 | Schematic diagrams illustrating procedures for generating composite maps and for assigning proteins to cryo-EM densities. a, Three local refinements (covering the SCMC, tubulin subcomplex, and PADI6 ring) were aligned to the consensus map and stitched with *volume maximum* in ChimeraX to generate a composite map of the asymmetric unit. Two copies of this asymmetric unit map were then aligned to an earlier consensus map (obtained before symmetry expansion) and stitched to generate a composite map of the globular repeat. Finally, three copies of this globular repeat map were fitted into the in situ subtomogram average from EMD-16458 and stitched to generate a composite map of the CPL filament. **b**, PADI6 and the core SCMC (NLRP5, TLE6, and OOEP) could be assigned based on direct similarity of the cryo-EM map to previously published structures. We noticed several unassigned densities associated with the SCMC proteins, for which we evaluated proteins with strong evidence of direct interaction with the SCMC from the literature, leading to confident assignment of KHDC3, ZBED3, and NLRP4F. Remaining densities were identified using a "visual proteomics" approach using SITUS/colores or DomainSeeker to automatically fit AlphaFold predictions of proteins identified in previously published oocyte proteomes, leading to the identification of tubulin, FBXW, NLRP14, UBE2, and UHRF1. **c**, To confirm protein assignments, we used CryoAtom to automatically build a model into the cryoEM density map, then used the resulting traces as inputs to either a fold-based search (in which FoldSeek was used to query the mouse AlphaFold database) or a sequence-based search (in which findMySequence was used to query the mouse proteome). See Methods for details.

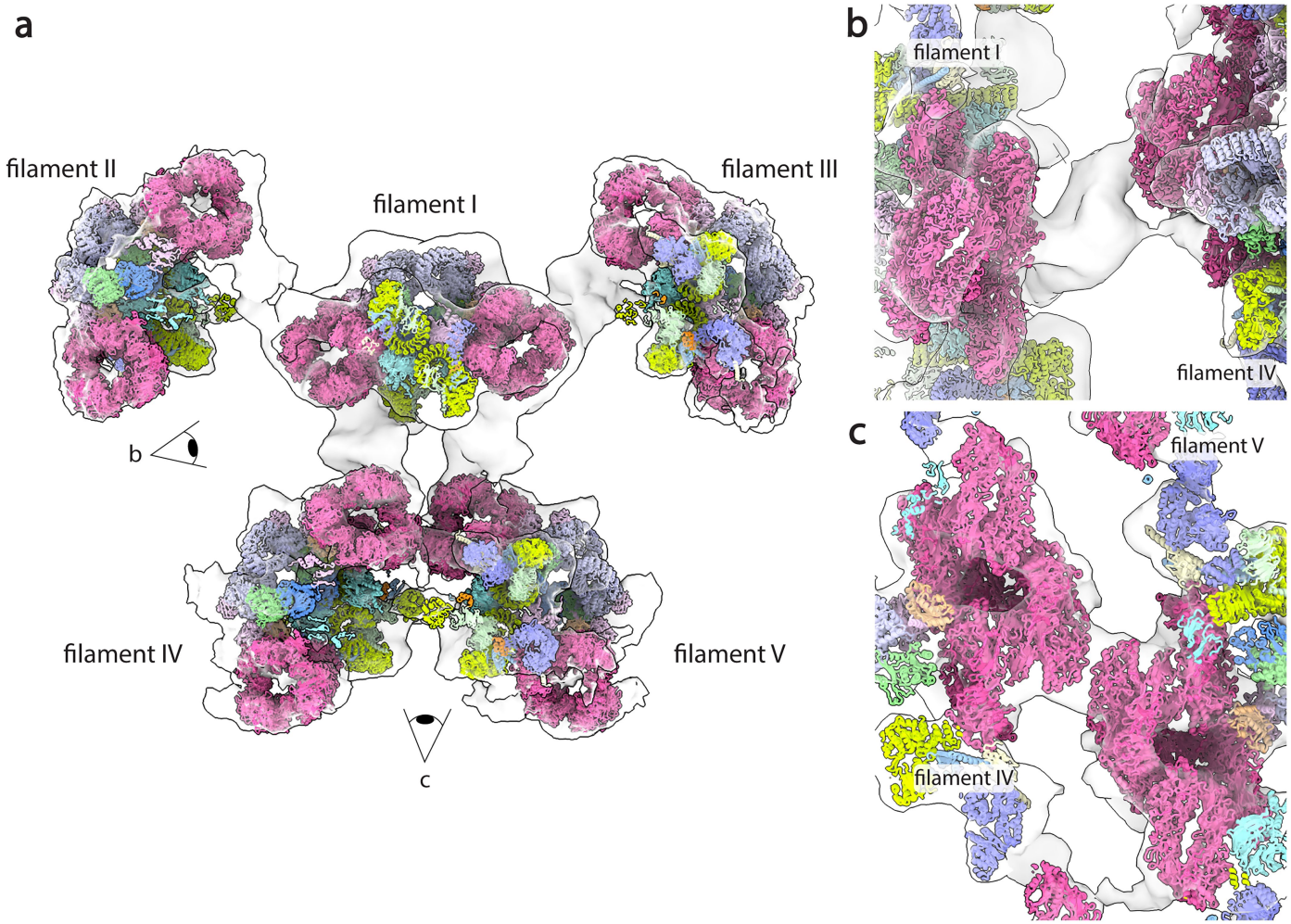


Extended Data Fig. 4 | See next page for caption.

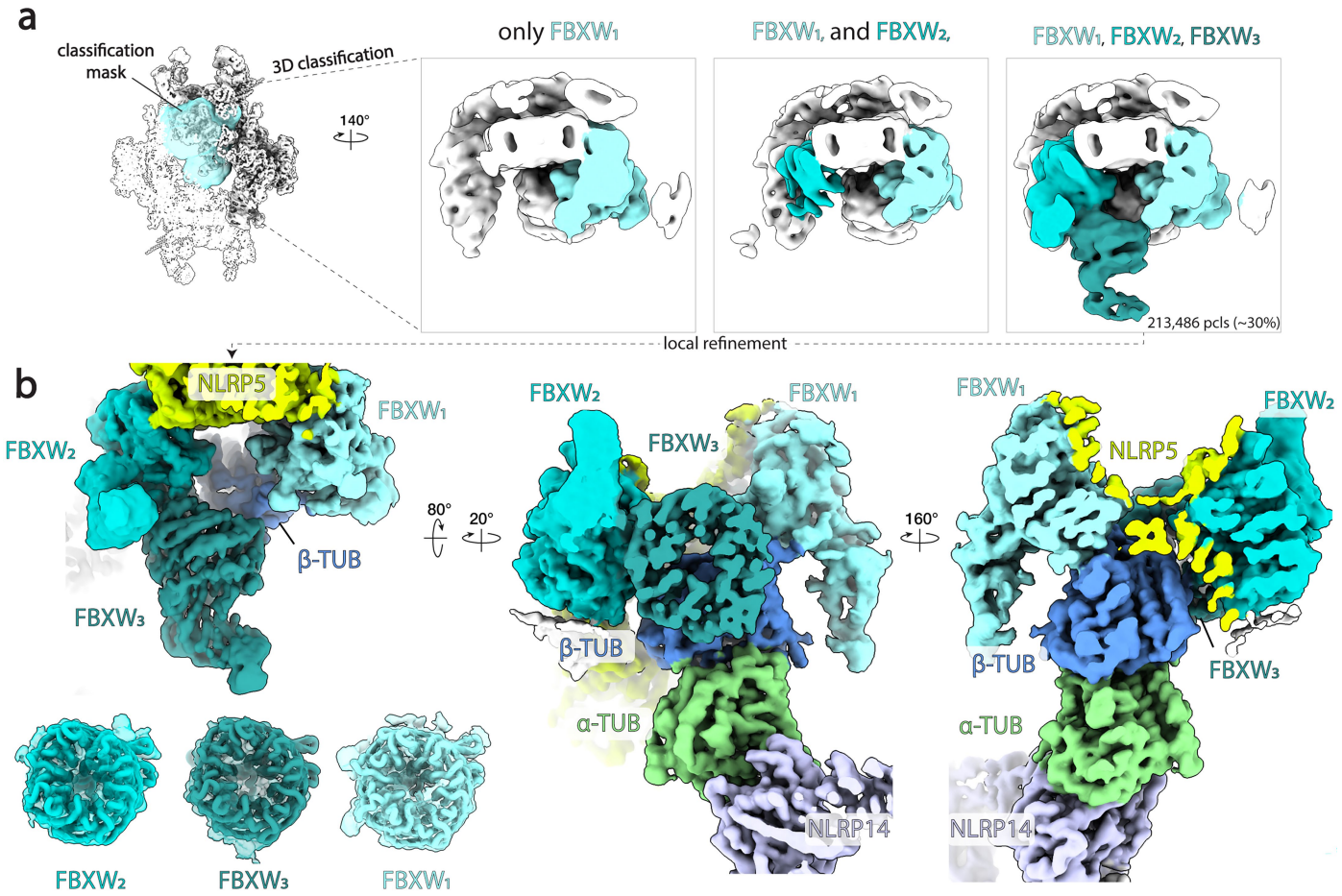
Extended Data Fig. 4 | Model-in-map fits of cytoplasmic lattice components and comparison of CPL-embedded PADI6 and SCMC with purified or reconstituted systems. a, Model-in-map fits of one CPL globular repeat (two asymmetric units). **b**, Model-in-map fits of individual CPL proteins. More detailed model-in-map fits and per-chain CC scores are shown in Supplementary Figs. 1–12. **c**, The CPL map obtained in this study by single-particle analysis (colored) is shown fitted into the CPL map obtained by subtomogram averaging (EMD-16458[1]). **d**, The atomic model of a PADI6 dimer from native mouse CPLs (pink, this study) is shown superimposed on crystal structures of a human PADI6 dimer (PDB 9FMN[26]) and a human PADI4 dimer (PDB 2DEW[27]). **e**, The atomic model of an SCMC dimer from native mouse CPLs (green, this study) is shown superimposed on cryo-EM-derived models of reconstituted mouse (PDB 8H93[33]) or human (PDB 8X7W[60]) SCMC core complexes. **f**, Graphical representation showing direct interactions among CPL components based on the cryo-EM data reported in this study.



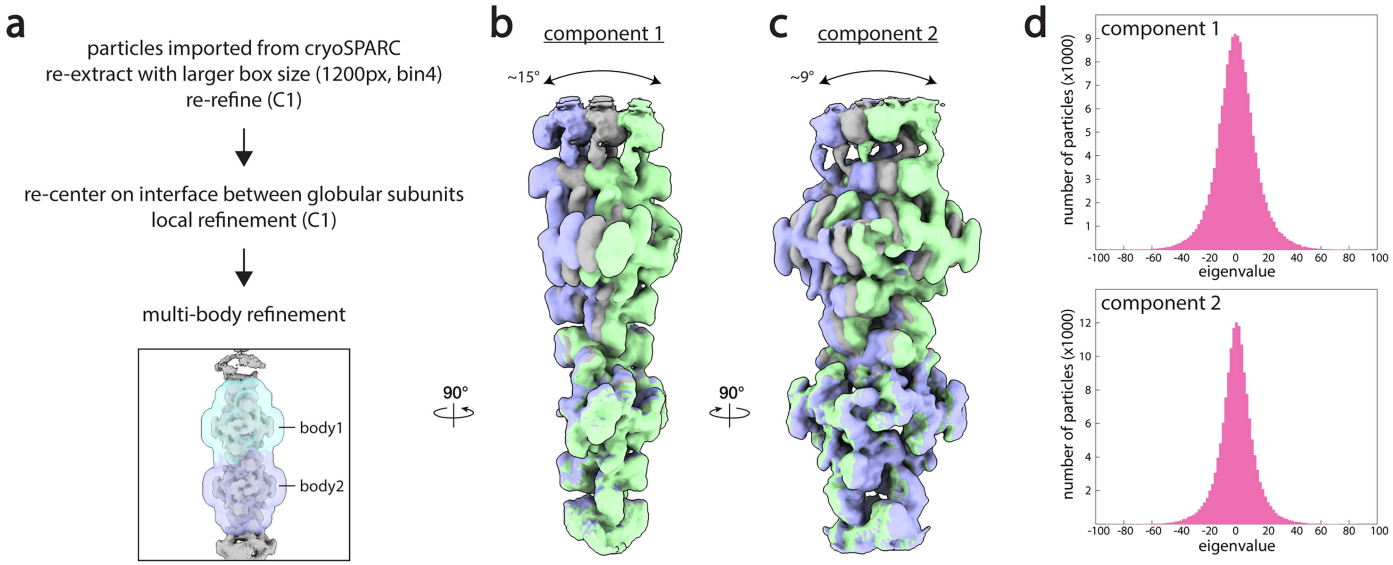
Extended Data Fig. 5 | Mass spectrometry of burst oocyte samples. **a**, Proteins identified in the burst oocyte preparation plotted according to their ranked median log_2-transformed iBAQ intensities across four replicates of ~30 oocytes each. Proteins identified in this study are colored (including all isoforms of tubulin, UBE2, and FBXW). **b**, Zoom-in of the most abundant proteins identified (with log_2IBAQ ≥ 18). Proteins modelled in our deposited structure are indicated with bold, colored font. The full list of identified proteins is provided in Supplementary Table 1.



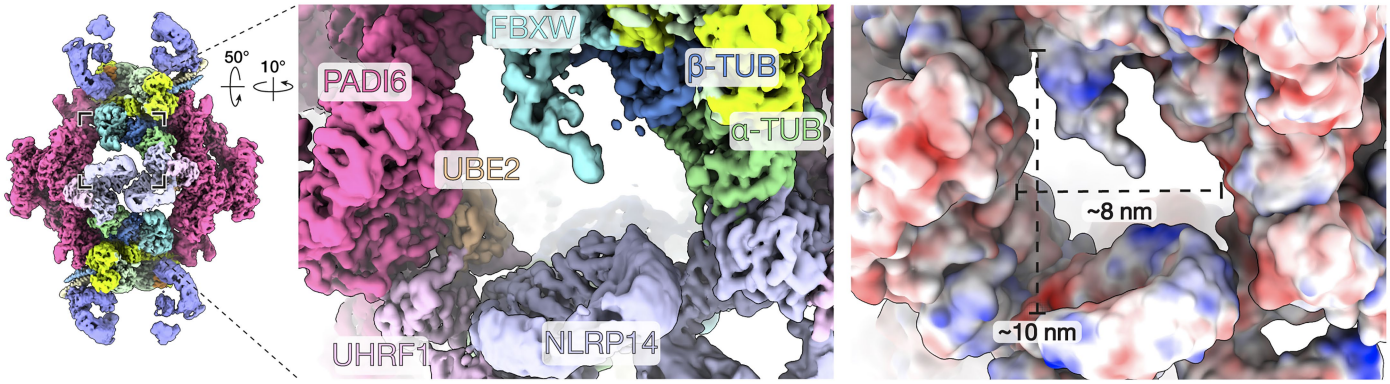
Extended Data Fig. 6 | PADI6 rings mediate interactions between individual CPL filaments within a bundle. a, Cross-section of an in situ subtomogram average of a CPL filament bundle (EMD-16458[1]) with multiple copies of our SPA-derived atomic models fitted. **b**, A "front-to-back" interface in which adjacent filaments are linked via as-yet-unidentified proteins bridging their PADI6 rings. **c**, A "back-to-back" interface in which the PADI6 rings of neighboring filaments appear to interact directly.



Extended Data Fig. 7 | FBXW proteins are abundant components of cytoplasmic lattices (CPLs). a, Three-dimensional classification without image alignment using a mask on the CPL asymmetric unit reveals classes with one, two, or three FBXW molecules bound. **b**, Cryo-EM density map after local refinement and post-processing demonstrating how FBXW proteins interact with NLRP5 and β-tubulin.



Extended Data Fig. 8 | Multi-body refinement reveals CPL conformational flexibility. a, To assess conformational flexibility, CPL particles imported from cryoSPARC into RELION-5 were re-extracted in with a large box size (1200 px, bin 4) and re-refined in C1. Particles were then re-centered on the interface between two subunits, re-extracted, and locally refined in C1. After local refinement, multi-body refinement was performed treating two adjacent globular repeats as two separate bodies. **b**,**c**, Analysis of the first two principal components (accounting for ~42% of the variance) revealed a forward/backward (b) and side-to-side (c) bending of one globular repeat relative to its neighbor. **d**, Unimodal histograms of the eigenvalues along the first two components are suggestive of continuous motion.



Extended Data Fig. 9 | PADI6, NLRP14, UHRF1, and UBE2 form a large pocket within the CPLs. Cryo-EM map (middle panel) and electrostatic properties (right panel) of the pocket. Assuming a sphere of diameter ~8-nm (volume of ~268 nm^3 or ~2.68 × 10^5 $Å^3$) and an average protein density of 1.43 g/cm^3 or ~0.861 Da/$Å^3$ [61,62], this pocket could accommodate a globular molecule ~230 kDa in size.

Extended Data Table 1 | Cryo-EM data collection, processing, and model building statistics

	native cytoplasmic lattices from mouse oocytes EMDB: EMD-54838 (composite), EMD-54839 (consensus), EMD-54840 to 54842 (local refinements) PDB: 9SFP	
Data collection and processing		
Microscope location and model	Netherlands Centre for Electron Nanoscopy (NeCEN), Titan Krios G1	
Accelerating voltage	300 kV	
Energy filter	Gatan BioQuantum	
Detector	Gatan K3	
Nominal magnification	81,000 X	
Electron exposure	50 e-/Å^2	
Nominal defocus range	-0.5 to -2.5 μm	
Pixel size	1.06 Å	
Initial number of movies	38,053	
Processing software	cryoSPARC v4.7.0, RELION-5	
Final number of particles	725,010 (consensus map after C2 symmetry expansion)	255,865 (PADI6 region after final Class3D)
	160,296 (SCMC region after final Class3D)	424,595 (tubulin subcomplex region after final Class3D)
FSC threshold	0.143	
Resolution estimate at FSC=0.143	4.2 (SCMC region), 4.1 (tubulin subcomplex region), 4.1 (PADI6 region)	
B-factor estimated in RELION (Å^2)	-112 (SCMC region), -135 (tubulin region), -140 (PADI6 region)	
Model building and refinement		
Resolution set in refinement (Å)	4.5	
Correlation coefficient CCvolume CCmask	 0.79 0.78	
Model composition Non-H atoms Protein residues Ligands	 117,355 14,769 0	
B-factors (Å^2)	151.97	
RMS deviations Bond length (Å) Bond angles (°)	 0.004 0.862	
Validation MolProbity score Clashscore Poor rotamers (%)	 1.72 6.83 0.02	
Ramachandran plot Favored (%) Allowed (%) Disallowed (%)	 95.08 4.91 0.01	

nature portfolio

Corresponding author(s): Miguel Leung, DPhil

Last updated by author(s): Mar 17, 2026

Reporting Summary

Nature Portfolio wishes to improve the reproducibility of the work that we publish. This form provides structure for consistency and transparency in reporting. For further information on Nature Portfolio policies, see our Editorial Policies and the Editorial Policy Checklist.

Statistics

For all statistical analyses, confirm that the following items are present in the figure legend, table legend, main text, or Methods section.

n/a	Confirmed
☐	☒ The exact sample size (*n*) for each experimental group/condition, given as a discrete number and unit of measurement
☒	☐ A statement on whether measurements were taken from distinct samples or whether the same sample was measured repeatedly
☒	☐ The statistical test(s) used AND whether they are one- or two-sided *Only common tests should be described solely by name; describe more complex techniques in the Methods section.*
☒	☐ A description of all covariates tested
☒	☐ A description of any assumptions or corrections, such as tests of normality and adjustment for multiple comparisons
☒	☐ A full description of the statistical parameters including central tendency (e.g. means) or other basic estimates (e.g. regression coefficient) AND variation (e.g. standard deviation) or associated estimates of uncertainty (e.g. confidence intervals)
☒	☐ For null hypothesis testing, the test statistic (e.g. *F*, *t*, *r*) with confidence intervals, effect sizes, degrees of freedom and *P* value noted *Give P values as exact values whenever suitable.*
☒	☐ For Bayesian analysis, information on the choice of priors and Markov chain Monte Carlo settings
☒	☐ For hierarchical and complex designs, identification of the appropriate level for tests and full reporting of outcomes
☒	☐ Estimates of effect sizes (e.g. Cohen's *d*, Pearson's *r*), indicating how they were calculated

Our web collection on statistics for biologists contains articles on many of the points above.

Software and code

Policy information about availability of computer code

Data collection	SerialEM v4.1, Warp v1.0.9
Data analysis	cryoSPARC v4.7.0, RELION v5.0, ChimeraX v1.10, LocScale-2.0, AlphaFold2, Phenix v1.20, Namdinator (no version number), Situs v3.8, DomainSeeker (no version number), CryoAtom v1.0.0, FoldSeek (no version number), findMySequence v1.0.12, pyem v0.66, Spectronaut v20.3

For manuscripts utilizing custom algorithms or software that are central to the research but not yet described in published literature, software must be made available to editors and reviewers. We strongly encourage code deposition in a community repository (e.g. GitHub). See the Nature Portfolio guidelines for submitting code & software for further information.

Data

Policy information about availability of data

All manuscripts must include a data availability statement. This statement should provide the following information, where applicable:

- Accession codes, unique identifiers, or web links for publicly available datasets
- A description of any restrictions on data availability
- For clinical datasets or third party data, please ensure that the statement adheres to our policy

Cryo-EM maps have been deposited to the EMDB with accession codes: EMD-54838 (composite map), EMD-54839 (consensus map), EMD-54840 (local refinement, PADI6 region), EMD-54841 (local refinement, SCMC region), and EMD-54842 (local refinement, tubulin subcomplex region). The atomic model has been deposited

to the PDB with accession code PDB 9SFP. Mass spectrometry data has been deposited in PRIDE with accession number PXD073451. Previously-published structures used for analysis/comparison include: EMD-16458, PDB 6DPV, PDB 4I4T, PDB 3CLZ, PDB 1FXT, PDB 9FMN, PDB 2DEW, PDB 8H93, and PDB 8X7W.

Research involving human participants, their data, or biological material

Policy information about studies with human participants or human data. See also policy information about sex, gender (identity/presentation), and sexual orientation and race, ethnicity and racism.

Reporting on sex and gender	N/A
Reporting on race, ethnicity, or other socially relevant groupings	N/A
Population characteristics	N/A
Recruitment	N/A
Ethics oversight	N/A

Note that full information on the approval of the study protocol must also be provided in the manuscript.

Field-specific reporting

Please select the one below that is the best fit for your research. If you are not sure, read the appropriate sections before making your selection.

☒ Life sciences ☐ Behavioural & social sciences ☐ Ecological, evolutionary & environmental sciences

For a reference copy of the document with all sections, see nature.com/documents/nr-reporting-summary-flat.pdf

Life sciences study design

All studies must disclose on these points even when the disclosure is negative.

Sample size	For cryo-EM processing, no methods were used to predetermine sample size because the final size of the cryo-EM datasets is dependent on what is necessary to obtain reconstructions at sufficient resolution to confidently identify proteins and build an atomic model. The exact number of micrographs/movies collected and particles used are listed in Extended Data Table 1. Mass spectrometry measurements were performed on four (4) independent replicates of ~30 oocytes each.
Data exclusions	Workflows for cryo-EM single particle reconstruction may down-weight or exclude particles.
Replication	The cryo-EM maps reported represent an average of several hundred thousand copies of the molecule of interest (exact particle numbers are given in Extended Data Table 1). Cryo-EM data in this study was collected from two different grids across two separate microscope sessions, with initial screening performed on independent biological preparations. Mass spectrometry measurements were performed on four (4) independent replicates of ~30 oocytes each; all mass spectrometry replicates were successful and yielded similar results.
Randomization	For calculation of Fourier Shell Correlation (FSC) curves used to estimate resolution, particles were randomly split into two half-sets during cryo-EM refinement. For mass spectrometry experiments, oocytes collected from several mice were randomly split into groups of ~30 oocytes each.
Blinding	No blinding was necessary and is not applicable to cryo-EM structure determination since no conditions/experimental treatments were being compared. Futhermore, knowledge of the proteins present within the sample is essential for building an accurate atomic model. Likewise, since conditions were not being compared, no blinding was done for mass spectrometry analysis.

Reporting for specific materials, systems and methods

We require information from authors about some types of materials, experimental systems and methods used in many studies. Here, indicate whether each material, system or method listed is relevant to your study. If you are not sure if a list item applies to your research, read the appropriate section before selecting a response.

Materials & experimental systems

n/a	Involved in the study
☒	☐ Antibodies
☒	☐ Eukaryotic cell lines
☒	☐ Palaeontology and archaeology
☐	☒ Animals and other organisms
☒	☐ Clinical data
☒	☐ Dual use research of concern
☒	☐ Plants

Methods

n/a	Involved in the study
☒	☐ ChIP-seq
☒	☐ Flow cytometry
☒	☐ MRI-based neuroimaging

Animals and other research organisms

Policy information about studies involving animals; ARRIVE guidelines recommended for reporting animal research, and Sex and Gender in Research

Laboratory animals	Oocytes were obtained from sexually-mature female BALB/cN mice. Ovaries were obtained exclusively from surplus animals sacrificed for other purposes.
Wild animals	The study did not involve wild animals.
Reporting on sex	Oocytes were collected from female animals.
Field-collected samples	The study did not involve samples collected from the field.
Ethics oversight	No ethical approval or guidance was required because organs were used from surplus animals sacrificed for other purposes.

Note that full information on the approval of the study protocol must also be provided in the manuscript.

Plants

Seed stocks	N/A
Novel plant genotypes	N/A
Authentication	N/A